Petroleum Science 19 (2022) 375–386

Contents lists available at ScienceDirect

Petroleum Science

journal homepage: www.keaipublishing.com/en/journals/petroleum-science

Hierarchically porous Beta/SBA-16 with different silica-alumina ratios and the hydrodesulfurization performances of DBT and 4,6-DMDBT

Jin-Lin Mei, Yu Shi, Cheng-Kun Xiao, Ao-Cheng Wang, Ai-Jun Duan**, Xi-Long Wang*

State Key Laboratory of Heavy Oil Processing, China University of Petroleum (Beijing), Beijing 102249, PR China

ARTICLE INFO

Article history:
Received 1 January 2021
Accepted 24 May 2021
Available online 15 October 2021

Edited by Xiu-Qiu Peng

Keywords:
Beta/SBA-16
Dibenzothiophene
4,6-Dimethyldibenzothiophene
Hydrodesulfurization

ABSTRACT

Hierarchically porous Beta/SBA-16 (BS) composite materials, combining the characteristics of the acidity from the Beta zeolite and the three-dimensional structure from SBA-16, were synthesized successfully through a two-step in-situ assembly hydrothermal crystallization method. A series of NiMo catalysts supported on BS with different silica-alumina ratios were prepared. The supports and the corresponding catalysts were characterized by XRD, N_2 physisorption, ^{27}Al MAS NMR, TEM, pyridine-FTIR, Raman, XPS and HRTEM. The activities of series catalysts were evaluated by the hydrodesulfurization (HDS) performances of dibenzothiophene (DBT) and 4,6-dimethyldibenzothiophene (4,6-DMDBT). It was found that the Beta crystallites were embedded into SBA-16 through silanols accompanied by dealumination on the T3–T9 sites of Beta crystallites. NiMo/BS-3 with a silica-alumina ratio of 100 exhibited the highest DBT and 4,6-DMDBT HDS activities at the WHSV value of 10 h^{-1}, with the conversions of 95.9% and 86.9% respectively, due to the synergistic effects of the suitable specific surface areas, the relatively large pore size, appropriate acidity, the relatively high sulfidation degree, moderate dispersity and good stacking degree of MoS_2 active phases.

1. Introduction

Environment protection has attracted more attention of the public, with the development of the economy. Especially the air pollution caused by automobile exhaust might result in great harm to the health of people. To solve this problem, many strict specifications for gasoline and diesel qualities were implemented in various countries. Sulfur content is one of the most important parameters, which is typically restricted to less than 10 ppm in American, Europe, and China. Researchers have developed multiple technologies to reduce the sulfur content in liquid fuels, including hydrodesulfurization (Schuman and Shalit, 1971; Vasudevanand Fierro, 1996), oxidative desulfurization (Wu et al. 2016, 2020; Zhang et al., 2020), adsorption desulfurization (Xiong et al., 2017; Khan et al., 2018), biodesulfurization (Watsuntorn et al., 2019) and extractive desulfurization (Song et al., 2017; Lima et al., 2018). Among them, hydrodesulfurization is the most effective method to remove sulfur. Industrial catalysts usually adopt alumina as support and MoS_2 promoted with Ni or Co as active phases (Méndez et al., 2017). However, the strong interaction between the traditional alumina and the active phase is not conducive to the formation of type II active phases with high activity (Hensen et al., 2002). Therefore, the macromolecular sulfur compound like 4,6-DMDBT is difficult to be removed with the traditional alumina based catalysts due to the steric hindrance of reactant (Zhang et al., 2010). The current research focuses on the development of high-efficiency hydrodesulfurization catalysts with large specific surface area, wide pore size, suitable acidity and good stacking degree of MoS_2. To enhance the conversion rate of refractory sulfur-containing compounds, silica and carbon materials with weaker metal-support interaction are used as supports (Hensen et al., 2001), and Brønsted acid sites are introduced to improve isomerization, dealkylation and C–C bond scission routes (Bej et al., 2004).

Since discovered in 1992, mesoporous silica materials have a wonderful future in the fields of catalysis (Na et al., 2011; Wei et al., 2012), adsorption (Li et al., 2003; Lee et al., 2005), separation (Brandhuber et al., 2005; Sun et al., 2011), sensors (Lu et al., 1997), hydrogen storage (Blin et al., 2001) and biomedicine (Niu et al., 2010), etc. (Stein et al., 2000; Wan et al., 2006). Mesoporous silica materials are also applied in the hydrodesulfurization (HDS) reaction because of their large pore volume, tunable pore size and

* Corresponding author.
** Corresponding author.
E-mail addresses: duanaijun@cup.edu.cn (A.-J. Duan), xilong.wang@kaust.edu.sa (X.-L. Wang).

https://doi.org/10.1016/j.petsci.2021.10.003

ordered structure. Vradman et al. (2003) loaded WS_2 onto SBA-15 to synthesize WS_2/SBA-15 catalysts. They found that WS_2 active phases were distributed on the mesoporous supports without blocking the channels. NiWS/SBA-15 catalysts with doping Ni into WS_2/SBA-15 displayed 1.4 times higher activity in the hydrodesulfurization of DBT and 7.3 times higher activity in the hydrogenation of toluene than those of commercial CoMo/Al_2O_3 catalysts. Soni et al. (2009) synthesized Mo/KIT-6, NiMo/KIT-6, and CoMo/KIT-6 catalysts, and they found that KIT-6 supported catalysts showed superior activities than those of γ-Al_2O_3 and SBA-15 because of three-dimensional mesopore connectivity favoring the diffusion of reactant and products.

However, there are also some drawbacks of mesoporous materials that limit their industrial applications. One of them is the poor hydrothermal stability of mesoporous materials derived from the amorphous pore walls. To enhance the hydrothermal stability of mesoporous materials, novel composites (Han et al., 2001; Zhang et al., 2010; Wu et al., 2014) in-situ assembled by zeolite seeds improve their framework configurations for different utilization purposes. Furthermore, the incorporation of zeolites also distinctly modulates the acidity of the composites.

Zeolite is wildly used in industrial applications (Bellussi et al., 1995; Feller et al., 2003) due to its acidity and stability. Zeolite Beta possesses three-dimensional connectivity with 12-membered rings as the minimum constricting apertures (Newsam et al., 1988). Therefore, zeolite Beta is considered to be a powerful candidate for synthesizing micro/mesoporous composites. Zhang et al. (2011) synthesized NiMo catalysts supported on Beta-SBA-15 which exhibited the highest DBT HDS activities than those catalysts supported Beta, SBA-15 and Al_2O_3. The prominent DBT HDS performances of NiMo/Beta-SBA-15 catalysts were attributed to the superior pore structure and large amounts of acid sites. NiMo catalysts (NiMo/BK) supported on Beta-KIT-6 (Zhang et al., 2010) showed higher DBT HDS activities than those of NiMo/KIT-6, NiMo/Beta, NiMo/SBA-15, and NiMo/Al_2O_3. Moreover, it was proposed that NiMo/KIT-6 exhibited higher activity than NiMo/SBA-15 because of the superior mass transfer ability of three-dimensional mesopore structure which coincides with the conclusion of Soni (Soni et al., 2009). Meanwhile, the suitable acidic properties enhanced the HDS activity of both direct desulfurization (DDS) and hydrogenation (HYD) reaction pathways, especially for DDS.

Similar to KIT-6, SBA-16 (Zhao et al., 1998) possesses a three-dimensional mesostructure which is favorable for the diffusion of reactants and products. Predictably, combining the acidity of Beta zeolite and the excellent texture properties of SBA-16 with three-dimensional mesostructured can produce a new material with outstanding HDS performance.

In this research, Beta-SBA-16 composite materials were synthesized by assembling of zeolite Beta seeds into the framework of SBA-16 under the hydrothermal condition. The NiMo/BS catalysts were synthesized by incipient wetness impregnation with aqueous solutions of ammonium molybdate and nickel nitrate. The physicochemical properties of supports and the corresponding sulfide catalysts were characterized by XRD, N_2 Physisorption, ^{27}Al MAS NMR, TEM, Raman, XPS and HRTEM. Beta-SBA-16 composites inherited the acidity of zeolite Beta and the three-dimensional mesopore connectivity of SBA-16. The interaction between zeolite Beta and mesoporous SBA-16 was discussed. Moreover, the distribution of Al sites and Al migration were investigated. The DBT and 4,6-DMDBT HDS activities were performed on the pilot fixed bed plant. The factors affecting DBT and 4,6-DMDBT HDS performance were also discussed.

2. Experimental

2.1. Synthesis of zeolite Beta seed

The zeolite Beta seed was synthesized through a hydrothermal method. Typically, a certain amount of tetraethylorthosilicate (TEOS, 28.4 wt% in SiO_2) was mixed with tetraethylammonium hydroxide (TEAOH, 25 wt%) in a flask to form the solution A. Subsequently, the solution B was prepared by blending sodium hydroxide (NaOH), sodium aluminate ($NaAlO_2$), TEAOH and 6 g deionized water in another container. Afterward, the solution B was dispersed into the solution A dropwise followed by constant stirring to generate a white sol with a ratio of $2Na_2O$:$1Al_2O_3$:30 SiO_2:2TEAOH. Finally, the sol was poured into an autoclave and crystallized at 140 °C for 24 h to obtain the zeolite Beta seed.

2.2. Synthesis of supports

In this process, triblock copolymer $EO_{106}PO_{70}EO_{106}$ (Pluronic F127) was used as a structure-directing agent and TEOS was used as a silica source. In a typical synthesis, 4 g F127 and 240 mL hydrochloric (HCl, 2 mol/L) were mixed under strong agitation for 4 h at 35 °C to obtain a homogeneous solution. Then, a particular amount of butanol serving as a cosurfactant was added to the solution. Whereafter, 16 g TEOS (28.4 wt% SiO_2) was dropwise interfused with the solution with continuous stirring for 2 h. Afterward, different amounts of the above-mentioned as-synthesized zeolite Beta seeds were dropwise added to these mixtures and stirred for another 1 h. These resulting mixtures were aged at 35 °C in static condition for 24 h before being transferred to Teflon-coated stainless-steel autoclaves and crystallized at 100 °C for 24 h. These materials were obtained by filtration, drying at 80 °C for 12 h and calcined at 550 °C for 6 h. The synthesized materials with different SiO_2/Al_2O_3 molar ratios (60, 80, 100, 120 and 140) by modulating the additions of zeolite Beta seed are denoted as BS-1, BS-2, BS-3, BS-4, and BS-5, respectively.

2.3. Synthesis of catalysts

Prior to the preparation of catalysts, ammonium exchange is essential to the activation of zeolites by ion exchange with ammonium chloride solution at 90 °C for 2 h. The series catalysts were prepared via impregnation as described in our previous work (Wang et al., 2016). The nominal compositions were 15.0 wt% of MoO_3 and 3.5 wt% of NiO. The corresponding NiMo catalysts were termed as NiMo/BS-1, NiMo/BS-2, NiMo/BS-3, NiMo/BS-4, and NiMo/BS-5, respectively.

2.4. Support and catalyst characterizations

The small-angle X-ray diffraction (SA-XRD) and wide-angle X-ray diffraction (WA-XRD) reflections were recorded on a Rigaku RINT D/Max-2500 powder X-ray diffractometer, using Cu Kα radiation ($\lambda = 0.15406$ nm, 40 Kv, 40 mA) with a goniometer speed of 1°/min. Textural characteristics were measured by Micromeritics Tristar II 3020 at −196 °C. The specific surface areas were calculated from the adsorption branch of the isotherms using the Brunauer–Emmett–Teller (BET) method. The pore size distributions were obtained by Barret–Joyner–Halenda (BJH) method. The total pore volumes were estimated by N_2 adsorption at a relative pressure of 0.98.^{27}Al solid-state magic-angle-spinning nuclear magnetic resonance spectroscopy (^{27}Al MAS NMR) measurements were performed on a Bruker Avance III 500 MHz spectrometer.

Transmission electron microscopy (TEM) was performed on a JEOL JEM-2100 at an acceleration voltage of 200 kV. The surface acidity of the catalysts was determined by pyridine-FTIR in an *in-situ* FTIR cell (MAGNAIR 560) with a resolution of 1 cm^{-1}. Raman spectra were measured on a Raman spectrometer (Renishaw Micro-Raman System, 2000) with a wavelength of 325 nm. The X-ray photoelectron spectra (XPS) were obtained on a Perkin Elmer PHI-1600 ESCA spectrometer using Al Kα radiation. The high-resolution transmission electron microscopy (HRTEM) studies of the sulfide catalysts were carried out using a microscope grid by a Philips Tecnai G2 F20 S-TWIN microscope at 300 kV. At least 300 crystallites were counted to determine the average slab length (L_{av}) and stacking number (N_{av}) according to the following equations:

$$L_{av} = \frac{\sum_{i=1}^{x} x_i L_i}{\sum_{i=1}^{x} x_i}, \quad (1)$$

$$N_{av} = \frac{\sum_{i=1}^{y} y_i N_i}{\sum_{i=1}^{y} y_i}. \quad (2)$$

Where x_i is the number of slabs with length L_i, and y_i is the number of slabs with stacking number N_i.

The average fraction of Mo atoms resided on the edge of the MoS_2 crystallites was donated as f_{Mo} which could be determined by equation (3):

$$f_{Mo} = \frac{\sum_{i=1}^{t} 6n_i - 6}{\sum_{i=1}^{t} 3n_i^2 - 3n_i + 1}. \quad (3)$$

In equation (3), it is assumed that the MoS_2 slabs are in perfect hexagons (Kasztelan et al., 1984). In this equation, n_i represents the number of Mo atoms in one edge determined by $n_i = L_{av}/6.4 + 0.5$. The numerator of equation (3) means the number of Mo atoms at the edge of the MoS_2 active phase, while the denominator is the total number of Mo atoms.

2.5. Catalytic activity

The HDS reaction of DBT and 4,6-DMDBT were performed in a fixed bed reactor (8 mm inner diameter and 400 mm in length) charged with 1 g catalysts (40–60 mesh). The catalysts were presulfided *in-situ* at 340 °C for 4 h in a stream of H_2 and 2 wt% CS_2 in cyclohexane solution under 4 MPa. The sulfur contents of reactants (DBT and 4,6-DMDBT in tetradecane) were 500 ppm. The reactions were carried out at 340 °C, 4 MPa with a H_2/oil ratio of 200 mL/mL. The sulfur contents of the reactants and products were measured by the sulfur and nitrogen analytical instrument (RPP-2000SN, Taizhou Central Analytical Instruments Co. Ltd., China). The HDS conversion of the catalysts was determined according to equation (4):

$$HDS(\%) = \frac{S_f - S_p}{S_f} \times 100\%. \quad (4)$$

Where S_f and S_p are the sulfur contents of the feedstock and the products, respectively.

3. Results

3.1. Characterization of supports

3.1.1. Powder X-ray diffraction

Fig. 1a and b shows the wide-angle and small-angle diffraction patterns for the calcined composites. Fig. 1a (f) exhibits intense reflections at $2\theta = 7.6°$ and 22.5°, meanwhile the weaker bands at 21.4°, 25.3°, 26.8°, 29.5°, and 43.7°, which are the typical features of zeolite Beta with the framework of *BEA. The diffraction patterns comprise both sharp and broad features because of highly fault structures in zeolite Beta, which influence the tortuosity of the pore connectivity along the ***c***-direction, but they show no impact on the accessible pore volume (Newsam et al., 1988). It is obvious that Fig. 1a (a–e) also exhibit two distinguishable peaks at 7.6° and 22.5° while others are not visible because of lower intensities, indicating the existence of zeolite Beta structure in the BS series materials. Besides, the peak intensities decrease gradually as the silica-alumina ratios increase, which agree well with the reduction of the contents of zeolite Beta seeds.

Fig. 1b shows the small-angle XRD patterns of the calcined supports with different silica-alumina ratios. All of these patterns exhibit a prominent intense peak at $2\theta = 0.8°$ corresponding to $d = 110$ Å that can be indexed as (110) Bragg reflection, indicating that they all have body-centered cubic SAB-16 ($Im\bar{3}m$) mesostructure. The lattice parameters are calculated to be $a = 156$ Å. The $d_{(110)}$ spacings reduced by 8 Å compared to that of pure calcined mesoporous silica SBA-16 (Zhao et al., 1998). That is, the lattice parameters a are smaller than the pure SBA-16 by 10 Å. The unit cell shrinks by 17%, which probably due to siloxane condensation. However, higher-order Bragg reflections are not resolved at $2\theta = 1.4–2.4°$. This would be attributed to small scattering domain sizes and the relatively weak forces of the neutral S^0I^0 templating route (Tanev, Pinnavaia, 1996). The reflection peaks become lower with the increasing contents of zeolite Beta seeds, meaning that the more addition of zeolite Beta seed is likely to reduce the orderliness of mesoporous SBA-16.

3.1.2. N_2 physisorption of supports

Fig. 2a and **b** shows the N_2 adsorption-desorption isotherms and pore size distributions of BS series supports, respectively. All the BS supports present type-IV isotherms, indicating that these supports possess a mesoporous structure similar to SBA-16. In addition, these supports display type-H2 hysteresis loops, the typical patterns of mesoporous SBA-16 materials with cage structure channels. Fig. 2b displays a single pulse at *ca.* 4.3 nm classified as mesopore, implying that the pore size is uniform for all of the micro-mesoporous materials. Furthermore, the intensities of the peaks become stronger along with the increase of the silica-alumina ratios, confirming that the pore distributions of the BS supports are more concentrated.

Table 1 shows the texture and structure characterization results of the BS supports. The results manifest that the assembling of zeolite Beta seed into the framework of BS composite makes a significant decrease in S_{BET} with the decrease of silica-alumina ratios. This can be ascribed to the obstruction of porous structure locally by zeolite Beta seed. Meanwhile, the pore volume is increasing gradually as the silica-alumina ratio increases. Furthermore, the pore sizes increase in the initial stage and then decline with the increase of silica-alumina ratios. Moreover, the pore sizes of the BS supports is much smaller than typical SBA-16 (54 Å) (Zhao et al., 1998), while the thickness of pore walls are higher than SBA-16 (112 Å).

3.1.3. ^{27}Al MAS NMR of supports

Fig. 3 shows the ^{27}Al NMR spectra of the BS supports and zeolite Beta. The intensive signal of zeolite Beta at 70–30 ppm is attributed to the tetrahedral aluminum species in the zeolite framework (Hannus et al., 1998). For the BS supports, the spectra exhibit another signal at around 0 ppm which comprises a sharp peak ascribed to the octahedral aluminum species and a broad peak

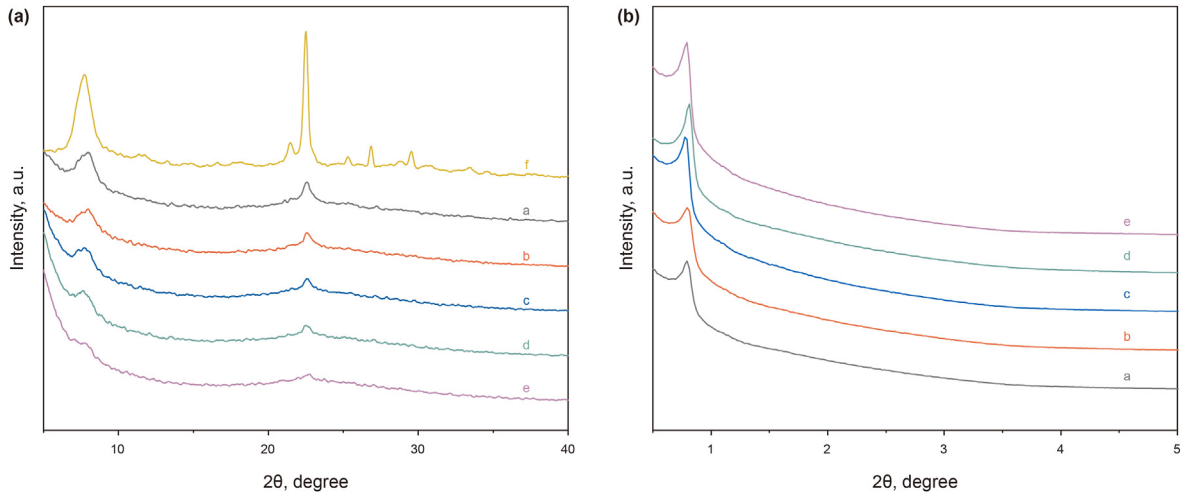

Fig. 1. (A) Wide-angle XRD patterns of BS series materials and zeolite beta seed (B) small-angle XRD patterns of supports: (a) BS-1; (b) BS-2; (c) BS-3; (d) BS-4; (e) BS-5; (f) zeolite beta.

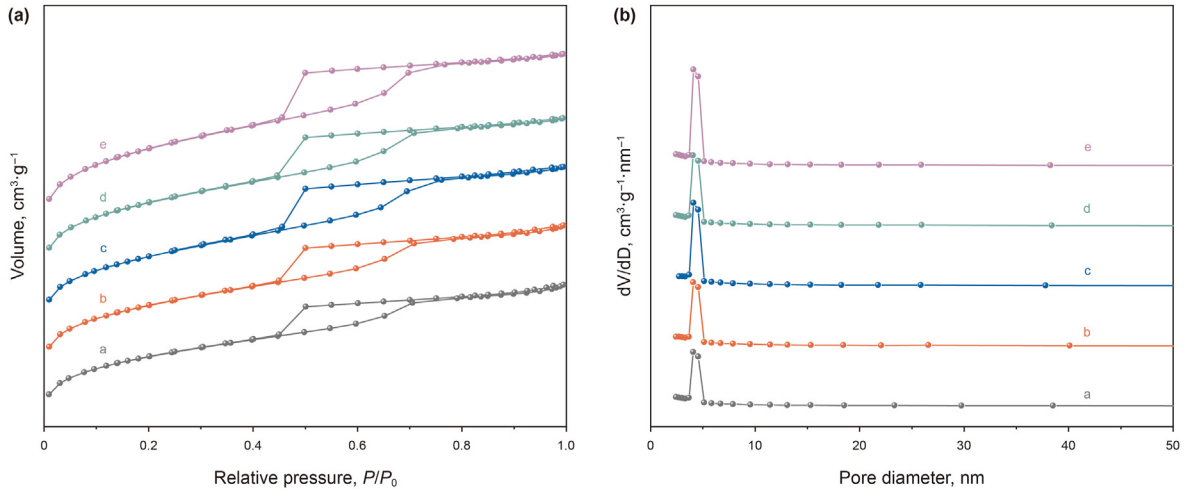

Fig. 2. (A) N_2 adsorption-desorption isotherms and (B) pore size distribution patterns of supports: (a) BS-1; (b) BS-2; (c) BS-3; (d) BS-4; (e) BS-5.

Table 1
Texture and structure characterization of the BS supports.

sample	S_{BET}, m^2/g[a]	V_p, cm^3/g[b]	$D_{ads\text{-}BJH}$, Å[c]	$d_{(110)}$, Å[d]	a, Å[e]	δ, Å[f]
BS-1	773	0.47	38.34	110.70	156.55	118.21
BS-2	792	0.51	38.43	109.99	155.55	117.12
BS-3	797	0.57	39.62	112.94	159.72	120.10
BS-4	830	0.56	38.06	108.83	153.91	115.85
BS-5	872	0.63	38.01	111.79	158.09	120.08

[a] Specific surface area determined by the BET method.
[b] Pore volume obtained by BJH adsorption cumulative volume of pores.
[c] Pore diameter determined from the adsorption branch of the isotherms by the BJH method.
[d] Interplanar spacing values $d_{(110)}$.
[e] Lattice parameter.$a = \sqrt{2} \cdot d_{(110)}$
[f] Pore wall thickness estimated as $\delta = a - D_{ads\text{-}BJH}$.

assigned to the distort octahedral aluminum species (Hannus et al., 1998; Maier et al., 2011; van Bokhoven et al., 2000). The formation of the number and type of octahedral aluminum species are affected by the method of calcination (Abraham et al., 2004). The stepwise calcination leads to a sharp framework-associated octahedral peak at around 0 ppm, while the calcination process in the presence of air will result in additional broad peaks. No signal attributable to the penta-coordinated aluminum or distorted tetrahedral aluminum is found at 30 ppm (Ibáñez et al., 2017; Schallmoser et al., 2014). The absolute intensity of peaks around 56 ppm decreases with the increase of the silica-alumina ratios as well as the peaks at around 0 ppm. Furthermore, the relative intensity of the octahedral aluminum species decreases with the enhancement of silica-alumina ratios, which is consistent with the previous reports (Pérez-Pariente et al., 1990; Abraham et al., 2004).

3.1.4. TEM images of supports

The TEM images of the BS supports are exhibited in Fig. 4. All of these supports display distinct long-range ordered structure. Fig. 4a and d shows the TEM images viewed along the [111] direction for BS-1 and BS-4, respectively, and Fig. 4b and e shows the TEM images viewed along the [110] direction for BS-2 and BS-5, correspondingly, while Fig. 4c is the viewed along the [001] direction for BS-3. The images in the top-right of Fig. 4a–e are corresponding FFT images. Therefore, all samples are confirmed to have the highly ordered body-centered cubic ($Im\bar{3}m$) mesostructured (Sakamoto et al., 2000), analogous to SBA-16. The blue structure models

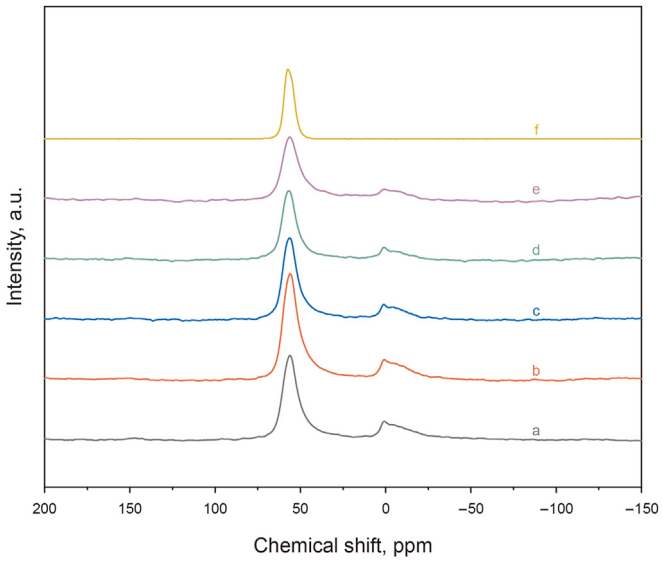

Fig. 3. ^{27}Al MAS NMR spectra of the BS supports and zeolite beta: (a) BS-1; (b) BS-2; (c) BS-3; (d) BS-4; (e) BS-5; (f) zeolite beta.

inside Fig. 4a–e represent the pore channels of SBA-16 viewed from different directions. The red lines are the borders of the models. The interplanar spacing of (110) of BS-3 estimated from Fig. 4c is 10.9 nm, in agreement with the result of small-angle XRD.

3.2. Characterization of catalysts

3.2.1. Pyridine-FTIR of the oxide catalysts

The acidities of the oxide catalysts were investigated by the pyridine-FTIR method using pyridine as a probe molecule. Fig. 5a and b shows the infrared spectra of the pyridine absorbed on the oxide catalysts in the region of 1700–1400 cm^{-1} subjected to thermal treatments at 200 °C and 350 °C, respectively. According to the literatures (Zhang et al., 2010), all the oxide catalysts exhibit many characteristic bands derived from pyridine bound to the Brønsted acid sites at 1639 and 1546 cm^{-1}, pyridine bound to the strong Lewis acid sites at 1609 and 1452 cm^{-1}, and a band at 1492 cm^{-1} which can be indexed to both Brønsted acid and Lewis acid sites. In addition, NiMo/BS-1 degassed at 200 °C shows the bands at 1623 and 1575 cm^{-1} due to the strong Lewis acid sites and the weak Lewis acid sites, accordingly. Furthermore, BS-2, BS-3, BS-4, and BS-5 degassed at 200 °C show a bond at 1596 cm^{-1} due to pyridine bound to silanol groups ≡SiOH. The relative intensities of absorption peaks decrease with the increase in silica-alumina ratios, except for the band at 1596 cm^{-1}. It is proposed that the numbers of the free silanol groups increase as the increase of the silica-alumina ratio. When the temperature of thermal treatments raises from 200 °C to 350 °C, the intensities of corresponding bands decrease, because the amount of absorbed pyridine decreases with higher thermal treatment temperature.

The acid strength distributions and the acid amounts are listed in Table 2. The results received at 200 °C are the total amounts of acid sites, while the results of 350 °C represent the amounts of the medium and strong acid sites. From the data in Table 2, the total acid and medium and strong acid amounts decrease gradually as the increase of the silica-alumina ratio, which is consistent with the results of the Al framework species in ^{27}Al NMR. The B/L ratios of total acid decrease gradually, while the B/L ratios of medium and strong acid increase at first and then decrease.

3.2.2. Raman of the oxide and sulfide catalysts

The Raman spectra of the oxide and sulfide catalysts of different silica-alumina ratios are presented in Fig. 6. Fig. 6a depicts the Raman spectra of the oxide catalysts. It is obvious that the dominant characteristic features are similar for all samples. The intensities of these bands, however, reflect the differences of the molybdenum species distributions of the individual samples. The most prominent band for all samples reside on ca. 960 cm^{-1} with a shoulder at 946 cm^{-1}, both of which are attributed to the symmetric stretching of terminal Mo═O bond in bridged or two-dimensional polymeric form of octahedral coordinated surface molybdenum species (Ferdous et al., 2007). The band at 946 cm^{-1} can be corresponding to the species of $Mo_7O_{24}^{6-}$ (Kim et al., 1994), which are considered to be highly dispersed and possess a weak interaction with the support, resulting in higher reducibility of the catalyst. The band at 960 cm^{-1} can be ascribed to large polymolybdate clusters such as $Mo_8O_{26}^{6-}$, which are believed to interact much strongly with the supports than $Mo_7O_{24}^{6-}$ (Jeziorowski, Knoezinger, 1979). The band at 900 cm^{-1} is due to the tetrahedral coordinated molybdenum species of MoO_4^{2-} (Ferdous et al., 2007). The occurrence of band at 825 cm^{-1} is assigned to Mo–O–Mo linkage of bulklike MoO_3 phase (Kunisada et al., 2004). Furthermore, the weak band at 1006 cm^{-1} is also originated from bulklike MoO_3, which is only perceptible in the NiMo/BS-1. The presence of bulklike MoO_3 implies the aggregation of molybdenum. It is remarkable that the proportion of polymolybdate shows a rising tendency at first and then declining as the silica-alumina ratios increase, while as it reaches a maximum as NiMo/BS-3. Base on the above results, it could be confirmed that NiMo/BS-3 are the most reducible catalyst which might possess higher HDS activity.

Fig. 6b depicts the Raman spectra of the sulfide catalysts. The apparent two bands at 380 cm^{-1} and 409 cm^{-1} are attributed to E^1_{2g} (out-of-plane vibration) and A_{1g} (in-plane vibration) phonon modes of MoS_2, respectively (Windom et al., 2011). E^1_{2g} mode is preferentially excited for basal bonding slabs due to the polarization dependence, while A_{1g} mode is preferentially excited for edge bonding slabs (Kong et al., 2013). The schematic of E^1_{2g} and A_{1g} vibrational modes is demonstrated inside of Fig. 6b. It is deduced that the base plans of the active phases prefer to parallel to the supports because the intensities of E^1_{2g} mode is close to that of A_{1g} mode for NiMo/BS serial catalysts (Seo et al., 2018). Corresponding to the Raman results of the oxide catalysts, the intensities of E^1_{2g} and A_{1g} vibration modes increase at first and then decrease as the silica-alumina ratio increase, indicating that NiMo/BS-3 possesses the highest sulfidation degree. The bands at 462 cm^{-1} are attributed to twice the LA(M) frequency of 231 cm^{-1} (Windom et al., 2011). The bands at 755 cm^{-1} are corresponding to twice the frequency of E^1_{2g}. It is more persuasive that the bands at 818 cm^{-1} are twice the A_{1g} mode of MoS_2 rather than a symmetric stretch of the terminal oxygen atoms of the bulk MoO_3, because the asymmetric stretches of the terminal oxygen atoms of MoO_3 at 995 cm^{-1} and wagging modes of the terminal oxygen atoms of MoO_3 at 285 cm^{-1} are not identifiable (Windom et al., 2011).

3.2.3. XPS of the sulfide catalysts

XPS measurements are used to characterize the chemical states and the composition of the sulfide catalysts. The representative spectra of Mo 3d are depicted in Fig. 7. The spectra were calibrated with C 1s peak at 284.6 eV as the standard in order to compensate for the sample charging. Generally, the 3d orbitals electrons possess apparently identifiable XPS signals for Mo species (Wang et al., 1997). Consequently, the molybdenum species can be quantified from the decomposition of Mo 3d spectra. The spin-orbit splitting of Mo 3d is 3.15 eV. The assignments of XPS signals are referred to the official website of the National Institute of Standards and

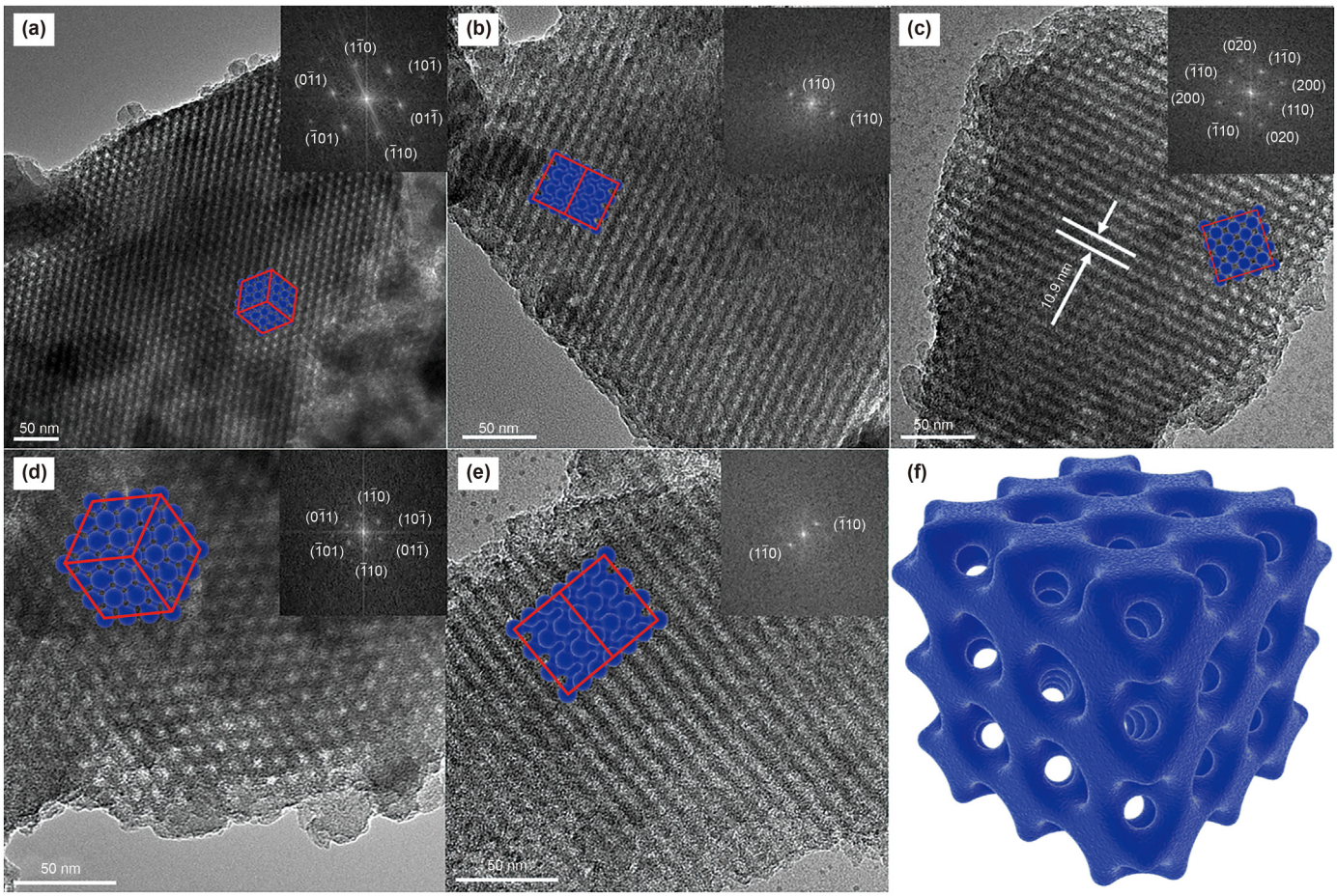

Fig. 4. TEM images of the BS supports and their Fourier diffractograms. (a) BS-1, viewed along the [111]; (b) BS-2, viewed along the [110]; (c) BS-3, viewed along the [001]; (d) BS-4, viewed along the [111]; (e) BS-5, viewed along the [110]; (f) structure model of BS composites. The inside images of a~e are the pore channels and FFT images of the corresponding supports.

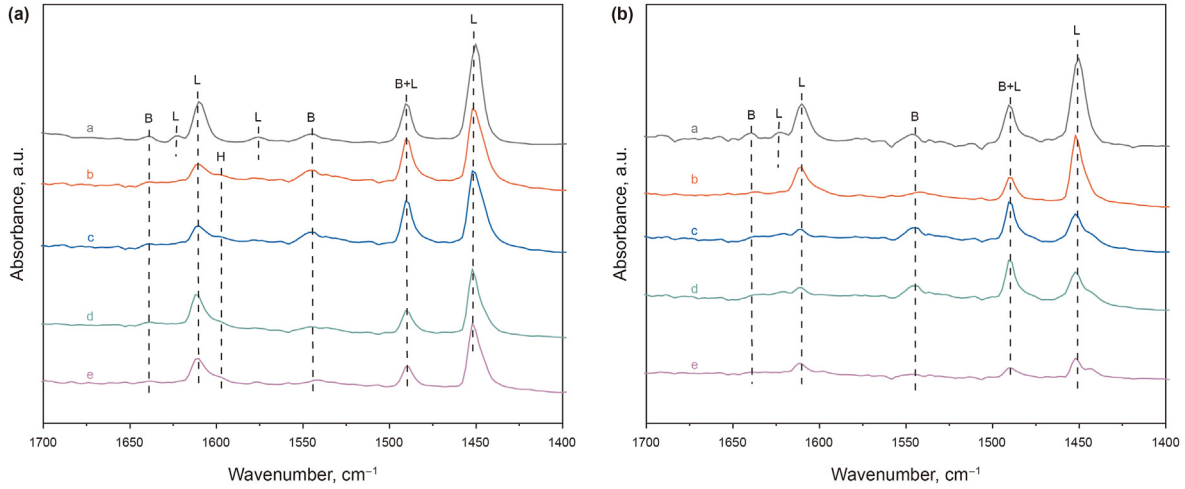

Fig. 5. FTIR-pyridine spectra of the oxidized catalysts: (a) NiMo/BS-1, (b)NiMo/BS-2, (c) NiMo/BS-3, (d) NiMo/BS-4, and (e) NiMo/BS-5 after degassing at (A) 200 °C and (B) 350 °C.

Technology (NIST) (NIST Standard Reference Database 20, Version 4.1). According to the Mo 3d spectra, there are three different oxidation degree Mo species including Mo(VI), Mo(V) and Mo(IV), which are attributed to the oxide, oxysulfide and sulfur phases respectively.

Table 3 depicts Mo 3d XPS results obtained from the series sulfide catalysts. Those peaks of Mo $3d_{5/2}$ binding energy (BE) at 228.8 ± 0.1 eV and Mo $3d_{3/2}$ at 231.9 ± 0.1 eV are corresponding to MoS_2, while the peaks of Mo $3d_{5/2}$ at 230.4 ± 0.1 eV and Mo $3d_{3/2}$ at 233.5 ± 0.1 eV are attributed to MoS_xO_y. Mo also exists as MoO_3

Table 2
Amounts of Brønsted and Lewis acid sites determined by pyridine-FTIR of the catalysts.

Catalysts	Amounts of acid sites, μmol·g^{-1}							
	200 °C				350 °C			
	L	B	L + B	B/L	L	B	L + B	B/L
BS-1	169.1	24.5	193.6	0.14	99.9	18.1	118.0	0.18
BS-2	147.5	17.6	165.1	0.12	53.1	10.2	63.3	0.19
BS-3	145.5	13.1	158.6	0.09	30.6	9.1	39.7	0.30
BS-4	129.3	5.6	134.9	0.04	20.3	2.8	23.1	0.14
BS-5	122.8	2.2	125.0	0.01	12.4	0.7	13.1	0.06

with Mo $3d_{5/2}$ peaks locating at 232.8 ± 0.1 eV and Mo $3d_{3/2}$ at 236.0 ± 0.1 eV. The remaining peaks at 226.2 eV represent S 2s of S^{2-}. There are no clear differences of BE of the corresponding Mo species and S species. The proportions of Mo(IV) are estimated from the peak area ratios of Mo(IV) to all Mo species. And the sulfidation degrees (S_{Mo}) are calculated from $S_{Mo} = Mo^{4+}/(Mo^{4+}+Mo^{5+}+Mo^{6+})$. As can be found in Table 3, the sulfidation degrees rise to the maximum of 51.1% of NiMo/BS-3 catalyst at first and then decline as the increase of the silica-alumina ratio, which agrees with the Raman results of the sulfide catalysts.

3.2.4. HRTEM of the sulfide catalysts

HRTEM was performed to examine the morphology of MoS_2 active phases. Representative micrographs of the sulfide catalysts are presented in Fig. 8. It is observed that all catalysts preserve MoS_2 crystallites in the typical layer structure with 6.2 Å interplanar distance. The histograms inset of Fig. 8a–e depicts the corresponding stacking number distributions of MoS_2 crystallites. Approximate 30% of MoS_2 crystallites have three layers and the stacking number distributions are extraordinary broad on all BS supports. Fig. 8f exhibits the length (L) distributions of MoS_2 slabs dispersed on BS supports. Over 40% of MoS_2 crystallites possess lengths within the scopes of 40 Å to 60 Å on all BS supports. The Average lengths and stacking numbers of MoS_2 crystallites of different catalysts are demonstrated in Table 4.

3.2.5. HDS results of DBT and 4,6-DMDBT

The activities of NiMo/BS series catalysts (see Table S1 and Table S2 in the supporting information) were evaluated in the HDS reactions of DBT and 4,6-DMDBT. Fig. 9 describes the efficiencies of DBT and 4,6-DMDBT HDS over NiMo/BS series catalysts at different WHSVs in the range of 10–100 h^{-1}. It is noteworthy that the efficiencies of both DBT and 4,6-DMDBT HDS were negative correlation with WHSV values because the contact times between the catalysts and the reactants prolong with the decrease of WHSV. It is found that the efficiencies of DBT HDS are higher than those of 4,6-DMDBT at all corresponding WHSVs because 4,6-DMDBT is more refractory derived from the steric hindrance of alkyl substitutes at 4,6-positions, which inhibit the intimate contact and the following reaction of S atoms with the metallic active sites. The activities of DBT and 4,6-DMDBT HDS over NiMo/BS series catalysts exhibit same increasing trend, NiMo/BS5 (85.28%, 73.48% at 10 h^{-1}) < NiMo/BS1 (89.39%, 75.83% at 10 h^{-1}) < NiMo/BS4 (91.35%, 79.53% at 10 h^{-1}) < NiMo/BS2 (92.13%, 83.02% at 10 h^{-1}) < NiMo/BS3 (95.88%, 86.88% at 10 h^{-1}). NiMo/BS-3 has the highest DBT and 4,6-DMDBT HDS activitives at the WHSV of 10 h^{-1}, with the HDS conversions of 95.9% and 86.9% respectively.

4. Discussion

The catalytic performances of DBT and 4,6-DMDBT HDS are affected by the characteristics of supports and metallic active phases, i.e., textural properties of supports, the acidity of the catalysts, the dispersity of active metal and the morphology of active phases.

In this research, Beta-SBA-16 composite materials were synthesized by an in-situ assembly hydrothermal method. The fabrication of Beta zeolite seeds into SBA-16 frameworks are confirmed by the characterization technologies of small-angle XRD, wide-angle XRD, and TEM. The coexistence of Beta zeolite and SBA-16 were proved by the results of wide-angle XRD and small-angle XRD in Fig. 1. The TEM images in Fig. 4 further validated the retained from its parent material structure of SBA-16. Combining the results of small-angle XRD in Fig. 1b and N_2 physisorption in Table 1, BS series materials had smaller pore sizes and unit cells and thicker pore walls than that of pure SBA-16. The shrink of unit cells ensured that the Beta zeolites were embedded into the pore walls of SBA-16, promoting the crosslinking of pore walls, while smaller pore sizes and thicker pore walls proofed that Beta zeolites had been embedded in the surfaces of channels in SBA-16.

In order to investigate the local environment of Al species deeply, ^{27}Al MAS NMR signals (see Fig. S1 in Supporting Information) were deconvoluted using Gaussian functions (Schallmoser

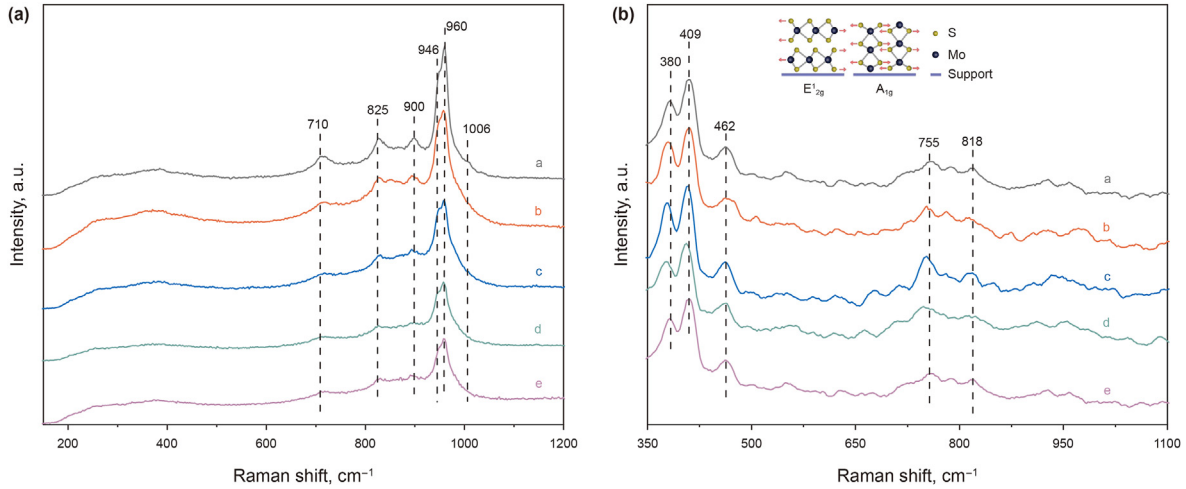

Fig. 6. Raman spectra of (A) the oxidized catalysts and (B) the sulfurized catalysts:(a) NiMo/BS-1, (b)NiMo/BS-2, (c) NiMo/BS-3, (d) NiMo/BS-4, and (e) NiMo/BS-5. The inset in (B) shows the atomic displacements of the E^1_{2g} and A_{1g} vibrational modes in bulk MoS_2 as viewed along the [1000] direction.

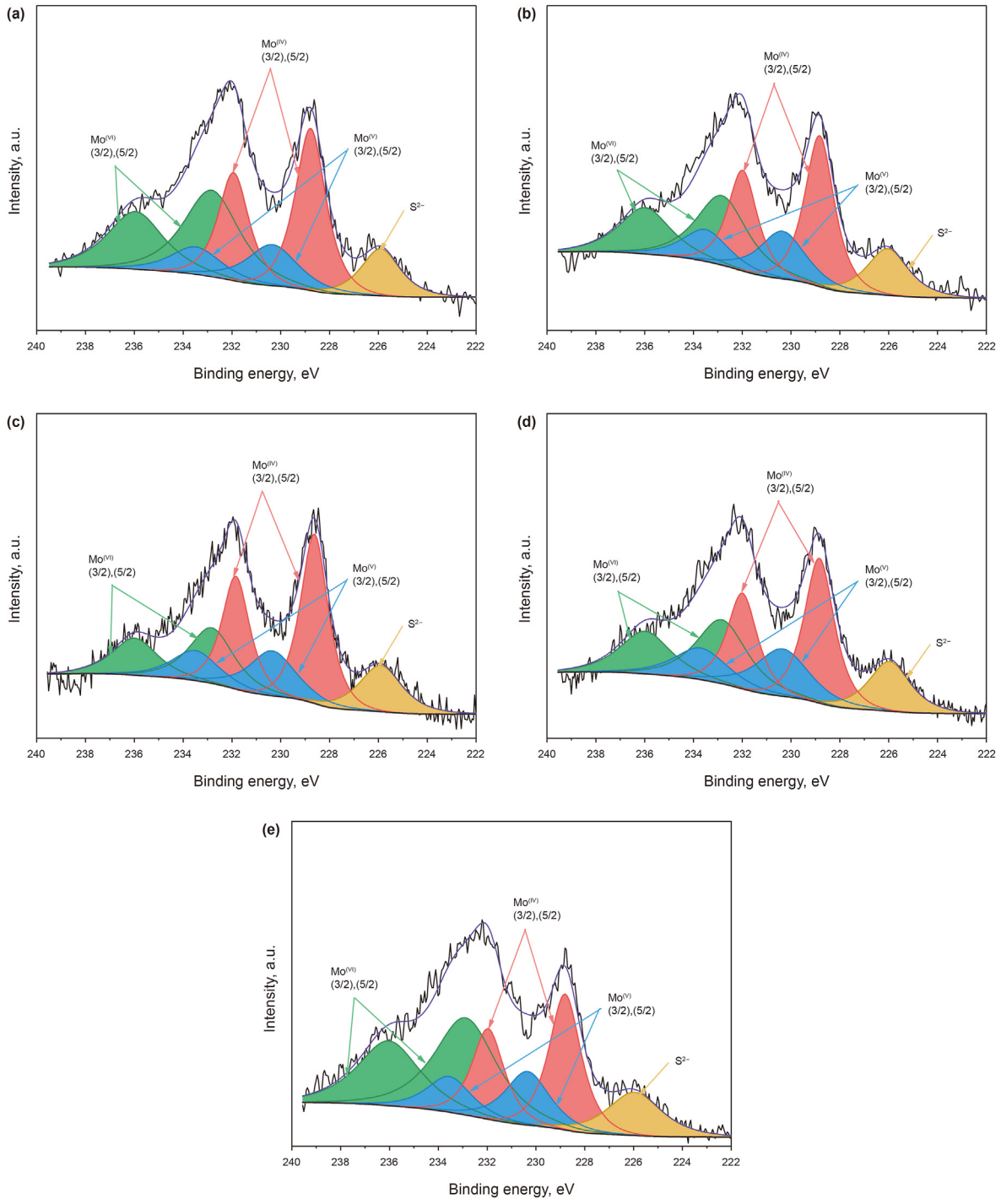

Fig. 7. Mo 3d XPS spectra of various sulfided catalysts:(A) NiMo/BS-1; (B) NiMo/BS-2; (C) NiMo/BS-3; (D) NiMo/BS-4; (E) NiMo/BS-5.

Table 3
Mo3d XPS results obtained from the series sulfide catalysts.

catalysts	Mo^{4+}		Mo^{5+}		Mo^{6+}		S_{Mo}
	ar. %	ar. %	ar. %	ar. %	ar. %	ar. %	
	228.8 ± 0.1 eV	231.9 ± 0.1 eV	230.4 ± 0.1 eV	233.5 ± 0.1 eV	232.8 ± 0.1 eV	236.0 ± 0.1 eV	
NiMo/BS-1	25	17	11	7	24	16	41.4
NiMo/BS-2	26	18	13	9	21	14	43.8
NiMo/BS-3	31	20	13	8	17	11	51.1
NiMo/BS-4	25	16	17	11	19	13	41.0
NiMo/BS-5	20	14	11	7	29	19	34.1

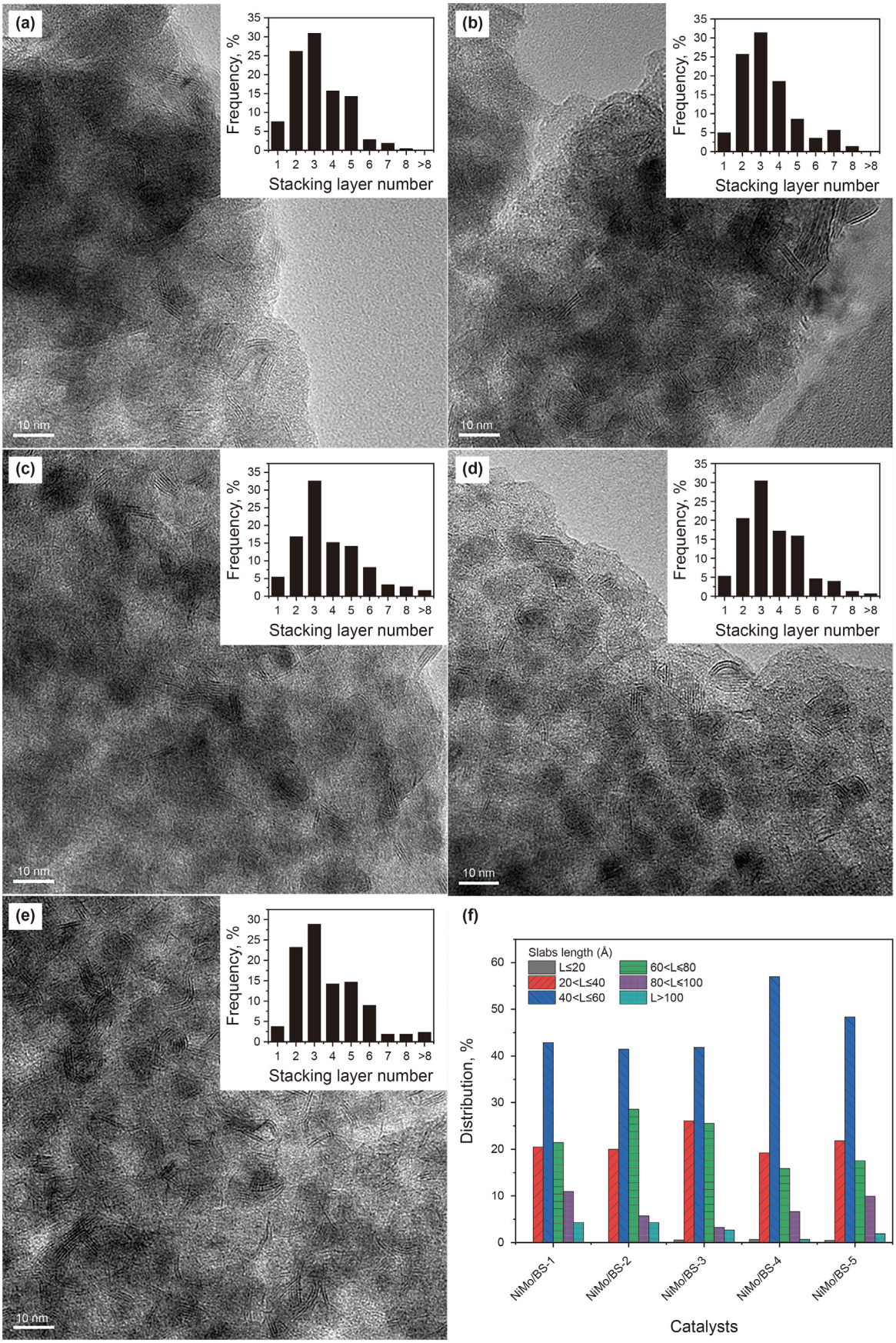

Fig. 8. HRTEM micrographs of NiMo/BS catalysts and the length distributions of MoS_2 slabs: (a) NiMo/BS-1, (b)NiMo/BS-2, (c) NiMo/BS-3, (d) NiMo/BS-4, (e) NiMo/BS-5 and (f) the length distributions of MoS_2 slabs.

Table 4
L_{av} and N_{av} of MoS_2 slabs over different catalysts.

catalyst	L_{av}, nm	N_{av}, nm	f_{Mo}
NiMo/BS-1	5.7	3.2	0.18
NiMo/BS-2	5.6	3.4	0.18
NiMo/BS-3	5.3	3.8	0.18
NiMo/BS-4	5.2	3.6	0.21
NiMo/BS-5	5.5	3.7	0.19

et al., 2014; Maier et al., 2011; van Bokhoven et al., 2000). The intensive signal at 70–30 ppm is an overlapping peak including four different Al species, while the signal at around 0 ppm contains a sharp peak and a broad peak. The results of deconvolution are listed in Table 5. As show in Table 5, the tetrahedral Al species consist of the distorted extra-framework Al species at 44 ppm, the framework Al species resided on T1 and T2 sites of Beta zeolite at 54 ppm, the framework Al species resided on T3–T9 sites of Beta zeolite at 57 ppm, and the extra-framework Al species at 63 ppm (Abraham et al., 2004; Maier et al., 2011). The octahedral Al species consist of the well-ordered octahedral Al species at 0 ppm and the distorted octahedral Al species at −8 ppm. Almost all of the Al species are the framework Al species in the Beta zeolite. Meanwhile, the amounts of Al species on T3–T9 sites account for 74% of the total Al species, which are about three times greater than that of Al species on T1 and T2 sites. Compared to the Beta zeolite, the proportions of Al species on T3–T9 sites in the BS composite materials are significantly reduced, while the proportions of Al species on T1 and T2 sites increase in some extent. As reflected in Fig. 3, the peak center of BS series materials moves toward the lower chemical shift than the pure Beta zeolite. It can be speculated that the Beta zeolite will be dealuminated at T3–T9 sites when it is incorporated with SBA-16, which might be derived from the acidic synthesis conditions of SBA-16 favorable for dealumination.

Silanol groups are identified by the peaks at 1596 cm^{-1} through pyridine-FTIR at 200 °C. Moreover, the peak intensity reduces gradually with the addition of Beta zeolite, meaning that more Beta zeolite accelerates the consumption of silanol groups. Combined with the foregoing discussions, it is inferred that Beta zeolite is embedded in the pores or incorporated into the pore wall of SBA-16 through interacting with Silanol groups, accompanied with dealumination. Comparing the results of pyridine-FTIR at 200 °C and 350 °C, it could be found that the corresponding B/L ratio is higher at 350 °C than that of 200 °C. It is deduced that the interaction between and Brønsted acids is stronger than that of Lewis acids (Corma, 1995). Therefore, it is more reasonable that most of the framework Al are still on the Beta skeleton, then Beta crystallites are fabricated into the pore walls of SBA-16.

The precursors of the active phases anchored on the supports in various forms including polymolybdate clusters, MoO_4^{2-} and MoO_3. The peak assigned to $Mo_7O_{24}^{6-}$ at 946 cm^{-1} represents for the specie that is prone to be sulfide. The proportion of MoO_3 bulk phase increases with the increase of silica-alumina ratio, which indicates the gradually weakened MSI. The most important precursor is $Mo_7O_{24}^{6-}$, which accounts of about half of the molybdenum species. Among all oxide catalysts, NiMo/BS-3 has the highest proportion of $Mo_7O_{24}^{6-}$. The results of Raman spectra of the sulfide catalysts also confirm that NiMo/BS-3 contains the highest MoS_2 active phases. Additionally, the results of XPS further confirm the highest sulfidation degree (51.1%) of NiMo/BS-3. The statistical results of HRTEM show that NiMo/BS-3 has moderate dispersity. Meanwhile, NiMo/BS-3 has the highest stacking number (3.8), which is facile to form NiMoS-II active phases (Van Veen et al., 1993). Furthermore, the suitable specific surface area of 797 m^2/g and the relatively

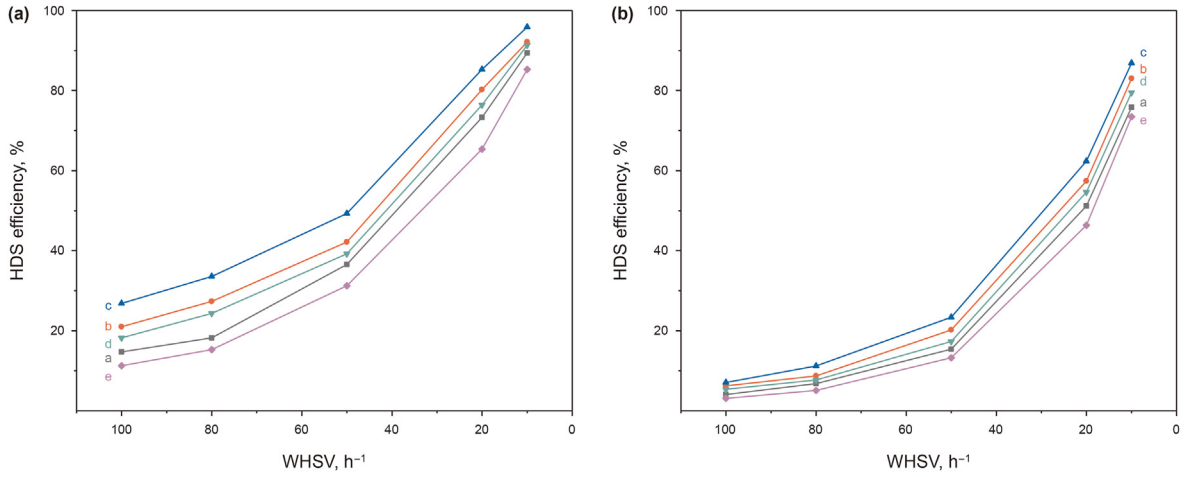

Fig. 9. HDS efficiencies of DBT (A) and 4,6-DMDBT (B) at different WHSVs over various catalysts: (a) NiMo/BS-1, (b)NiMo/BS-2, (c) NiMo/BS-3, (d) NiMo/BS-4, and (e) NiMo/BS-5.

Table 5
Deconvolution results of ^{27}Al MAS NMR.

Samples	Tetrahedral aluminum				Octahedral aluminum	
	44 ppm (%) EFAl	54 ppm (%) T1, T2 sites	57 ppm (%) T3–T9 sites	63 ppm (%) EFAl	0 ppm (%) EFAl	−8 ppm (%) EFAl
Beta	0	23	74	3	0	0
BS-1	14	29	29	9	4	15
BS-2	15	34	29	5	4	13
BS-3	15	29	33	6	6	11
BS-4	10	27	38	8	5	12
BS-5	13	37	31	6	4	8

large pore size of 4.0 nm will benefit to the diffusion of reactants and products inside the pores of catalysts.

In summary, the synergistic effects of the outstanding textural properties, suitable acidity, appropriate dispersion and morphology of MoS_2 active phases contribute collectively to the excellent DBT and 4,6-DMDBT HDS performance of NiMo/BS-3.

5. Conclusion

Hierarchical porous Beta/SBA-16 composite materials, which combined the advantages of Beta zeolite and SBA-16, were synthesized successfully. It is found that Beta crystallites were assembled into the pore walls of SBA-16. More than half of Al species attributed to T3–T9 sites of Beta zeolite was shifted because of the acidic synthesis conditions. The decrease of silanols with the silica-alumina ratio increasing demonstrated that Beta crystallites were embedded into SBA-16 through Silanol groups.

The DBT and 4,6-DMDBT HDS performances of various catalysts changed in the sequence of NiMo/BS5 < NiMo/BS1 < NiMo/BS4 < NiMo/BS2 < NiMo/BS3. NiMo/BS-3 exhibited the highest DBT and 4,6-DMDBT HDS activities (95.88%, 86.88% at 10 h^{-1}) due to the synergistic effects of the suitable specific surface areas, the relatively large pore size, appropriate acidity, relatively high sulfidation degree, moderate dispersity and morphology of MoS_2 phases.

Acknowledgment

This research was supported by the National Natural Science Foundation of China (No. 21878330, 21676298), the National Science and Technology Major Project (No. 2019YFC1907700), the CNPC Key Research Project (2016E-0707), and the King Abdullah University of Science and Technology (KAUST).

Appendix A. Supplementary data

Supplementary data to this article can be found online at https://doi.org/10.1016/j.petsci.2021.10.003.

References

Abraham, A., Lee, S.-H., Shin, C.-H., Bong Hong, S., Prins, R., van Bokhoven, J.A., 2004. Influence of framework silicon to aluminium ratio on aluminium coordination and distribution in zeolite Beta investigated by ^{27}Al MAS and ^{27}Al MQ MAS NMR. Phys. Chem. Chem. Phys. 6 (11), 3031. https://doi.org/10.1039/b401235f.

Bej, S.K., Maity, S.K., Turaga, U.T., 2004. Search for an efficient 4, 6-DMDBT hydrodesulfurization catalyst: a review of recent studies. Energy Fuel. 18 (5), 1227–1237. https://doi.org/10.1021/ef030179+.

Bellussi, G., Pazzuconi, G., Perego, C., Girotti, G., Terzoni, G., 1995. Liquid-phase alkylation of benzene with light olefins catalyzed by β-zeolites. J. Catal. 157 (1), 227–234. https://doi.org/10.1006/jcat.1995.1283.

Blin, J., Léonard, A., Su, B., 2001. Synthesis of large pore disordered MSU-type mesoporous silicas through the assembly of $C_{16}(EO)_{10}$ surfactant and TMOS silica source: effect of the hydrothermal treatment and thermal stability of materials. J. Phys. Chem. B 105 (26), 6070–6079. https://doi.org/10.1021/jp0036442.

Brandhuber, D., Torma, V., Raab, C., Peterlik, H., Kulak, A., Hüsing, N., 2005. Glycol-modified silanes in the synthesis of mesoscopically organized silica monoliths with hierarchical porosity. Chem. Mater. 17 (16), 4262–4271. https://doi.org/10.1021/cm048483j.

Corma, A., 1995. Inorganic solid acids and their use in acid-catalyzed hydrocarbon reactions. Chem. Rev. 95 (3), 559–614. https://doi.org/10.1021/cr00035a006.

Feller, A., Guzman, A., Zuazo, I., Lercher, J.A., 2003. 9 A novel process for solid acid catalyzed isobutane/butene alkylation. In: Anpo, M., Onaka, M., Yamashita, H. (Eds.), Studies in Surface Science and Catalysis. Elsevier, pp. 67–72.

Ferdous, D., Bakhshi, N.N., Dalai, A.K., Adjaye, J., 2007. Synthesis, characterization and performance of NiMo catalysts supported on titania modified alumina for the hydroprocessing of different gas oils derived from Athabasca bitumen. Appl. Catal. B Environ. 72 (1–2), 118–128. https://doi.org/10.1016/j.apcatb.2006.10.008.

Han, Y., Xiao, F.-S., Wu, S., Sun, Y., Meng, X., Li, D., et al., 2001. A novel method for incorporation of heteroatoms into the framework of ordered mesoporous silica materials synthesized in strong acidic media. J. Phys. Chem. B 105 (33), 7963–7966. https://doi.org/10.1021/jp011204k.

Hannus, I., Konya, Z., Nagy, J.B., Lentz, P., Kiricsi, I., 1998. Solid state MAS NMR investigation of Y-type zeolites reacted with chlorofluorocarbons. Appl. Catal. B Environ. 17 (1–2), 157–166. https://doi.org/10.1016/S0926-3373(98)00009-5.

Hensen, E., Kooyman, Pv, Van der Meer, Y., Van der Kraan, A., De Beer, V., Van Veen, J., et al., 2001. The relation between morphology and hydrotreating activity for supported MoS_2 particles. J. Catal. 199 (2), 224–235. https://doi.org/10.1006/jcat.2000.3158.

Hensen, Ed, De Beer, V., Van Veen, J., Van Santen, R., 2002. A refinement on the notion of type I and II (Co) MoS phases in hydrotreating catalysts. Catal. Lett. 84 (1), 59–67. https://doi.org/10.1023/A:1021024617582.

Ibáñez, M., Epelde, E., Aguayo, A.T., Gayubo, A.G., Bilbao, J., Castaño, P., 2017. Selective dealumination of HZSM-5 zeolite boosts propylene by modifying 1-butene cracking pathway. Appl. Catal. Gen. 543, 1–9. https://doi.org/10.1016/j.apcata.2017.06.008.

Jeziorowski, H., Knoezinger, H., 1979. Raman and ultraviolet spectroscopic characterization of molybdena on alumina catalysts. J. Phys. Chem. 83 (9), 1166–1173. https://doi.org/10.1021/j100472a012.

Kasztelan, S., Toulhoat, H., Grimblot, J., Bonnelle, J., 1984. A geometrical model of the active phase of hydrotreating catalysts. Appl. Catal. 13 (1), 127–159. https://doi.org/10.1016/S0166-9834(00)83333-3.

Khan, N.A., Bhadra, B.N., Jhung, S.H., 2018. Heteropoly acid-loaded ionic liquid@metal-organic frameworks: effective and reusable adsorbents for the desulfurization of a liquid model fuel. Chem. Eng. J. 334, 2215–2221. https://doi.org/10.1016/j.cej.2017.11.159.

Kim, D.S., Wachs, I.E., Segawa, K., 1994. Molecular structures and reactivity of supported molybdenum oxide catalysts. J. Catal. 149 (2), 268–277. https://doi.org/10.1006/jcat.1994.1295.

Kong, D., Wang, H., Cha, J.J., Pasta, M., Koski, K.J., Yao, J., et al., 2013. Synthesis of MoS_2 and $MoSe_2$ films with vertically aligned layers. Nano Lett. 13 (3), 1341–1347. https://doi.org/10.1021/nl400258t.

Kunisada, N., Choi, K.-H., Korai, Y., Mochida, I., Nakano, K., 2004. Novel zeolite based support for NiMo sulfide in deep HDS of gas oil. Appl. Catal. Gen. 269 (1–2), 43–51. https://doi.org/10.1016/j.apcata.2004.03.051.

Lee, J., Kim, J., Kim, J., Jia, H., Kim, M.I., Kwak, J.H., et al., 2005. Simple synthesis of hierarchically ordered mesocellular mesoporous silica materials hosting crosslinked enzyme aggregates. Small 1 (7), 744–753. https://doi.org/10.1002/smll.200500035.

Li, Y., Shi, J., Hua, Z., Chen, H., Ruan, M., Yan, D., 2003. Hollow spheres of mesoporous aluminosilicate with a three-dimensional pore network and extraordinarily high hydrothermal stability. Nano Lett. 3 (5), 609–612. https://doi.org/10.1021/nl034134x.

Lima, F., Gouvenaux, J., Branco, L.C., Silvestre, A.J., Marrucho, I.M., 2018. Towards a sulfur clean fuel: deep extraction of thiophene and dibenzothiophene using polyethylene glycol-based deep eutectic solvents. Fuel 234, 414–421. https://doi.org/10.1016/j.fuel.2018.07.043.

Lu, Y., Ganguli, R., Drewien, C.A., Anderson, M.T., Brinker, C.J., Gong, W., et al., 1997. Continuous formation of supported cubic and hexagonal mesoporous films by sol–gel dip-coating. Nature 389 (6649), 364. https://doi.org/10.1038/38699.

Maier, S.M., Jentys, A., Lercher, J.A., 2011. Steaming of zeolite BEA and its effect on acidity: a comparative NMR and IR spectroscopic study. J. Phys. Chem. B 115 (16), 8005–8013. https://doi.org/10.1021/jp108338g.

Méndez, F.J., Franco-López, O.E., Bokhimi, X., Solís-Casados, D.A., Escobar-Alarcón, L., Klimova, T.E., 2017. Dibenzothiophene hydrodesulfurization with NiMo and CoMo catalysts supported on niobium-modified MCM-41. Appl. Catal. B Environ. 219, 479–491. https://doi.org/10.1016/j.apcatb.2017.07.079.

Na, K., Jo, C., Kim, J., Cho, K., Jung, J., Seo, Y., et al., 2011. Directing zeolite structures into hierarchically nanoporous architectures. Science 333 (6040), 328–332.

Newsam, J., Treacy, M.M., Koetsier, W., Gruyter, Cd, 1988. Structural characterization of zeolite Beta. Proceedings of the royal society of London. A. mathematical and physical sciences 420 (1859), 375–405. https://doi.org/10.1098/rspa.1988.0131.

NIST standard reference Database 20. Version 4.1. https://srdata.nist.gov/xps/.

Niu, D., Ma, Z., Li, Y., Shi, J., 2010. Synthesis of core-shell structured dual-mesoporous silica spheres with tunable pore size and controllable shell thickness. J. Am. Chem. Soc. 132 (43), 15144–15147. https://doi.org/10.1021/ja1070653.

Pérez-Pariente, J., Sanz, J., Fornés, V., Corma, A., 1990. ^{29}Si and ^{27}Al MAS NMR study of zeolite β with different Si/Al Ratios. J. Catal. 124 (1), 217–223. https://doi.org/10.1016/0021-9517(90)90116-2.

Sakamoto, Y., Kaneda, M., Terasaki, O., Zhao, D.Y., Kim, J.M., Stucky, G., et al., 2000. Direct imaging of the pores and cages of three-dimensional mesoporous materials. Nature 408 (6811), 449. https://doi.org/10.1038/35044040.

Schallmoser, S., Ikuno, T., Wagenhofer, M.F., Kolvenbach, R., Haller, G.L., Sanchez-Sanchez, M., et al., 2014. Impact of the local environment of Brønsted acid sites in ZSM-5 on the catalytic activity in n-pentane cracking. J. Catal. 316, 93–102. https://doi.org/10.1016/j.jcat.2014.05.004.

Schuman, S., Shalit, H., 1971. Hydrodesulfurization. Catal Rev. 4 (1), 245–318. https://doi.org/10.1080/01614947108075491.

Seo, B., Jung, G.Y., Kim, J.H., Shin, T.J., Jeong, H.Y., Kwak, S.K., et al., 2018. Preferential horizontal growth of tungsten sulfide on carbon and insight into active sulfur sites for the hydrogen evolution reaction. Nanoscale 10 (8), 3838–3848. https://doi.org/10.1039/c7nr08161h.

Song, Z., Zhou, T., Qi, Z., Sundmacher, K., 2017. Systematic method for screening ionic liquids as extraction solvents exemplified by an extractive desulfurization process. ACS Sustain. Chem. Eng. 5 (4), 3382–3389. https://doi.org/10.1021/

acssuschemeng.7b00024.
Soni, K., Rana, B.S., Sinha, A.K., Bhaumik, A., Nandi, M., Kumar, M., et al., 2009. 3-D ordered mesoporous KIT-6 support for effective hydrodesulfurization catalysts. Appl. Catal. B Environ. 90 (1–2), 55–63. https://doi.org/10.1016/j.apcatb.2009.02.010.
Stein, A., Melde, B.J., Schroden, R.C., 2000. Hybrid inorganic-organic mesoporous silicates—nanoscopic reactors coming of age. Adv. Mater. 12 (19), 1403–1419. https://doi.org/10.1002/1521-4095(200010)12:19<1403::AID-DMA1403>3.0.CO;2-X.
Sun, Z., Deng, Y., Wei, J., Gu, D., Tu, B., Zhao, D., 2011. Hierarchically ordered macro-/mesoporous silica monolith: tuning macropore entrance size for size-selective adsorption of proteins. Chem. Mater. 23 (8), 2176–2184. https://doi.org/10.1021/cm103704s.
Tanev, P.T., Pinnavaia, T.J., 1996. Mesoporous silica molecular sieves prepared by ionic and neutral surfactant templating: a comparison of physical properties. Chem. Mater. 8 (8), 2068–2079. https://doi.org/10.1021/cm950549a.
van Bokhoven, J.A., Koningsberger, D., Kunkeler, P., Van Bekkum, H., Kentgens, A., 2000. Stepwise dealumination of zeolite βeta at specific T-sites observed with ^{27}Al MAS and ^{27}Al MQ MAS NMR. J. Am. Chem. Soc. 122 (51), 12842–12847. https://doi.org/10.1021/ja002689d.
Van Veen, J., Colijn, H., Hendriks, P., Van Welsenes, A., 1993. On the formation of type I and type II NiMoS phases in NiMo/Al_2O_3 hydrotreating catalysts and its catalytic implications. Fuel Process. Technol. 35 (1–2), 137–157. https://doi.org/10.1016/0378-3820(93)90089-M.
Vasudevan, P., Fierro, J.G., 1996. A review of deep hydrodesulfurization catalysis. Catal. Rev. 38 (2), 161–188. https://doi.org/10.1080/01614949608006457.
Vradman, L., Landau, M., Herskowitz, M., Ezersky, V., Talianker, M., Nikitenko, S., et al., 2003. High loading of short WS_2 slabs inside SBA-15: promotion with nickel and performance in hydrodesulfurization and hydrogenation. J. Catal. 213 (2), 163–175. https://doi.org/10.1016/S0021-9517(02)00012-X.
Wan, Y., Yang, H., Zhao, D., 2006. "Host-Guest" chemistry in the synthesis of ordered nonsiliceous mesoporous materials. Accounts Chem. Res. 39 (7), 423–432. https://doi.org/10.1021/ar050091a.
Wang, H., Skeldon, P., Thompson, G., 1997. XPS studies of MoS_2 formation from ammonium tetrathiomolybdate solutions. Surf. Coating. Technol. 91 (3), 200–207. https://doi.org/10.1016/S0257-8972(96)03186-6.
Wang, X., Zhao, Z., Zheng, P., Chen, Z., Duan, A., Xu, C., et al., 2016. Synthesis of NiMo catalysts supported on mesoporous Al_2O_3 with different crystal forms and superior catalytic performance for the hydrodesulfurization of dibenzothiophene and 4,6-dimethyldibenzothiophene. J. Catal. 344, 680–691. https://doi.org/10.1016/j.jcat.2016.10.016.
Watsuntorn, W., Ruangchainikom, C., Rene, E.R., Lens, P.N., Chulalaksananukul, W., 2019. Comparison of sulphide and nitrate removal from synthetic wastewater by pure and mixed cultures of nitrate-reducing, sulphide-oxidizing bacteria. Bioresour. Technol. 272, 40–47. https://doi.org/10.1016/j.biortech.2018.09.125.
Wei, J., Yue, Q., Sun, Z., Deng, Y., Zhao, D., 2012. Synthesis of dual-mesoporous silica using non-ionic diblock copolymer and cationic surfactant as co-templates. Angew. Chem. 124 (25), 6253–6257. https://doi.org/10.1002/anie.201202232.
Windom, B.C., Sawyer, W.G., Hahn, D.W., 2011. A Raman spectroscopic study of MoS_2 and MoO_3: spplications to tribological systems. Tribol. Lett. 42 (3), 301–310. https://doi.org/10.1007/s11249-011-9774-x.
Wu, H., Duan, A., Zhao, Z., Li, T., Prins, R., Zhou, X., 2014. Synthesis of NiMo hydrodesulfurization catalyst supported on a composite of nano-sized ZSM-5 zeolite enwrapped with mesoporous KIT-6 material and its high isomerization selectivity. J. Catal. 317, 303–317. https://doi.org/10.1016/j.jcat.2014.07.002.
Wu, P., Lu, L., He, J., Chen, L., Chao, Y., He, M., et al., 2020. Hexagonal boron nitride: a metal-free catalyst for deep oxidative desulfurization of fuel oils. Green Energy Environ 5 (2), 166–172. https://doi.org/10.1016/j.gee.2020.03.004.
Wu, P., Zhu, W., Chao, Y., Zhang, J., Zhang, P., Zhu, H., et al., 2016. A template-free solvent-mediated synthesis of high surface area boron nitride nanosheets for aerobic oxidative desulfurization. Chem. Commun. 52 (1), 144–147. https://doi.org/10.1039/C5CC07830J.
Xiong, J., Li, H., Yang, L., Luo, J., Chao, Y., Pang, J., et al., 2017. Metal-free boron nitride adsorbent for ultra-deep desulfurization. AlChE J 63 (8), 3463–3469. https://doi.org/10.1002/aic.15695.
Zhang, D., Duan, A., Zhao, Z., Wang, X., Jiang, G., Liu, J., et al., 2011. Synthesis, characterization and catalytic performance of meso-microporous material Beta-SBA-15-supported NiMo catalysts for hydrodesulfurization of dibenzothiophene. Catal. Today 175 (1), 477–484. https://doi.org/10.1016/j.cattod.2011.03.060.
Zhang, D., Duan, A., Zhao, Z., Xu, C., 2010. Synthesis, characterization, and catalytic performance of NiMo catalysts supported on hierarchically porous Beta-KIT-6 material in the hydrodesulfurization of dibenzothiophene. J. Catal. 274 (2), 273–286. https://doi.org/10.1016/j.jcat.2010.07.012.
Zhang, M., Liu, J., Li, H., Wei, Y., Fu, Y., Liao, W., et al., 2020. Tuning the electrophilicity of vanadium-substituted polyoxometalate based ionic liquids for high-efficiency aerobic oxidative desulfurization. Appl. Catal. B Environ. 271, 118936. https://doi.org/10.1016/j.apcatb.2020.118936.
Zhao, D., Huo, Q., Feng, J., Chmelka, B.F., Stucky, G.D., 1998. Nonionic triblock and star diblock copolymer and oligomeric surfactant syntheses of highly ordered, hydrothermally stable, mesoporous silica structures. J. Am. Chem. Soc. 120 (24), 6024–6036. https://doi.org/10.1021/ja974025i.